Chemical Science

ROYAL SOCIETY OF CHEMISTRY

EDGE ARTICLE

View Article Online
View Journal | View Issue

Cite this: *Chem. Sci.*, 2025, **16**, 7004

All publication charges for this article have been paid for by the Royal Society of Chemistry

Received 30th January 2025
Accepted 14th March 2025

DOI: 10.1039/d5sc00812c

rsc.li/chemical-science

P≡B and As≡B triple bonds in the linear PB_2O^- and AsB_2O^- species†

Han-Wen Gao, Jie Hui and Lai-Sheng Wang *

Due to its electron deficiency, boron triple bonds are relatively scarce. We use high-resolution photoelectron imaging to investigate the structures and bonding of the EB_2O^- (E = P, As) type of clusters, which are found to have [E≡B–B≡O]$^-$ closed-shell linear structures with E≡B triple bonds. The B atoms in the linear EB_2O^- species undergo sp hybridization, while the E atoms also undergo sp hybridization to form a σ bond with the sp orbital of B along with two π bonds formed by the p_x and p_y orbitals. The high-resolution photoelectron imaging data reveal detachment transitions from the EB_2O^- ($^1\Sigma^+$) anions to the EB_2O ($^2\Pi$) neutrals. The electron affinities of PB_2O and AsB_2O are measured to be 3.592(1) eV and 3.432(1) eV, respectively; the vibrational frequencies for the E–B, B–B, and B–O stretching modes are measured for both species. The spin–orbit splitting of the $^2\Pi$ state to $^2\Pi_{3/2}$ and $^2\Pi_{1/2}$ is measured to be 153 cm^{-1} and 758 cm^{-1} for PB_2O and AsB_2O, respectively.

1. Introduction

Borylene (:BR) is the boron analogue of carbene (:CR_2).[1] The HOMO of borylene is an sp hybridized σ-type orbital, while the LUMO and LUMO+1 are the two empty p (p_x and p_y) orbitals. Compared with carbenes, borylenes are more reactive due to their two vacant p orbitals. This also makes borylenes better π-acceptors and they can be stabilized by favourable back-donation of d electrons from transition metals. The first borylene complex was synthesized within the ligand sphere of a stable transition metal complex in 1998 with the form of L_nMBR.[2] Since then, many borylene complexes have been synthesized.[3] Owing to their ability to form π bonds by the two vacant p orbitals, borylenes have the potential to form triple bonds with transition metals. Transition metal–boron triple-bond characters were first hinted in the [$(OC)_5$Cr=$BSi(SiMe_3)_3$] complex,[3f] in which the Cr–B bond length is slightly shorter than a Cr=B double bond. The shortest transition metal–boron bond length was reported in an L_nFeBF compound[4] with an Fe–B bond length comparable to the Fe≡B triple-bond. Transition metal–boron triple bonds have been observed in the linear ReB_2O^- and IrB_2O^- gaseous anions.[5] Interestingly, RhB_2O^- was found to have a bent structure with a short Rh–B bond, leading to the discovery of the first Rh≡B quadruple bond.[6] These gaseous anions were produced by laser vaporization, in which the stable BO boronyl unit was readily formed due to trace amounts of oxygen contaminants, serving as a convenient monovalent substituent in the simple borylene model of :B–BO.

In contrast to transition metal–boron complexes, main group elements are more challenging to form triple bonds with boron due to the absence of d electrons. However, the B≡B triple bond can be formed using donor ligands, such as in [OC → B≡B ← CO] or the first isolated B≡B stabilized by two bulky carbenes.[7] If B acquires an electron, B^- is isoelectronic to C and can form B≡B triple bonds, such as in the dianion [OB–B≡B–BO]$^{2-}$ and [Bi≡B–BO]$^-$ or the recent Bi≡BH^- species.[8–10] Triple bonds between group 15 elements with boron are particularly interesting because they are analogous to C≡C triple bonds. Numerous iminoborane R–N≡B–R′ moieties featuring a N≡B triple bond have been synthesized, as evidenced by their linear structures and short N–B bond lengths.[11] However, as one moves down the periodic table, R–E≡B–R′ type compounds start to exhibit bent structures, especially on the R–E side.[12] For example, the simplest HPBH molecule, which is isoelectronic with alkynes, is predicted to be bent,[13] indicating a P–B bond order lower than three. The bending is a result of less s-orbital overlap as one descends the periodic table.[12,14] The reduced s orbital contribution by the E atom in the RE side leads to a shift from sp to sp^2 hybridization, transforming the geometry from linear to bent. In sp^2 hybridization, only one p orbital remains available to form a π bond. Equivalently, in the MO picture under the bent geometry, the in-plane π bonding orbital has the same symmetry as the antibonding σ orbital. This leads to significant mixing between the two orbitals, weakening the in-plane π bond and making it more like a lone pair, consistent with the valence bond perspective. Thus, the bent geometry inherently reduces the bond order below three. The few synthesized phosphaborene (R–P=B–R′) and

Department of Chemistry, Brown University, Providence, RI 02912, USA. E-mail: lai-sheng_wang@brown.edu

† Electronic supplementary information (ESI) available. See DOI: https://doi.org/10.1039/d5sc00812c

arsaborene (R–As=B–R′) molecules are found to exhibit bent geometries with P=B and As=B double bonds.[15]

Thus, it is challenging to synthesize molecules with P≡B or As≡B triple bonds. No compounds with such triple bonds have been isolated in the bulk except a theoretical suggestion of a P≡B triple bond protected by bulky groups.[16] Alternatively, molecules containing P≡B or As≡B triple bonds can be prepared in the gas phase or low temperature matrices, where it is possible to form linear molecules with bare P or As atoms unprotected by ligands. The PBH radical was observed in a low temperature matrix, an open-shell species with three π electrons and a P–B bond order of 2.5.[17] In this article, we use high-resolution photoelectron imaging (PEI) to study EB_2O^- (E = P, As) clusters produced by a laser vaporization source. High-resolution photoelectron spectra from photoelectron imaging (PEI) of cryogenically cooled anions and theoretical calculations confirm that the EB_2O^- species are electron-precise linear molecules, $[E{\equiv}B{-}B{\equiv}O]^-$, containing a terminal E≡B triple bond (E = P, As). The electron affinities (EAs), vibrational frequencies, and spin–orbit (SO) splitting of the neutral EB_2O radicals are obtained for the first time.

2. Experimental and theoretical methods

2.1. Experimental methods

The experiment was carried out on a high-resolution PEI apparatus newly equipped with a cryogenically cooled 3D Paul trap. The PEI apparatus has been described in detail previously,[18] and has been proven to be effective to cool anionic clusters generated from a laser vaporization source.[19] In the current work, the PB_2O^- and AsB_2O^- clusters were produced by laser vaporization of cold-pressed P/^{10}B and As/^{10}B targets, respectively. The boronyl species were generated due to trace amounts of oxide impurity on the target surface. In fact, the PB_2O^- and AsB_2O^- clusters were particularly prominent in the mass spectra, indicating that they are highly stable thermodynamically. A helium carrier gas was used to quench the laser-induced plasma. Clusters formed inside the nozzle were entrained by the helium carrier gas and underwent a supersonic expansion. After passing through a skimmer, the collimated cluster beam travelled directly into the 3D Paul trap cooled down to 4.2 K by a two-stage closed-cycle helium refrigerator. Clusters of interest were selected and intercepted by a detachment laser in the interaction zone of a velocity map imaging (VMI) system. Photodetachment was performed using the frequency-doubled output of a dye laser, as well as the third harmonic output from an Nd:YAG laser. Photoelectrons were projected onto a set of microchannel plates coupled with a phosphor screen and a charge-coupled-device camera. The VMI lens was calibrated using PEI of Bi^- at various photon energies. The photoelectron images were analysed by the maximum entropy method (MEVELER).[20] The resolution of the VMI system was ~0.6% for electrons with high kinetic energies and as low as 1.2 cm^{-1} for very slow photoelectrons.[18]

Photoelectron angular distributions (PADs) can be obtained from photoelectron images, characterized by an anisotropy parameter (β). Under the electric dipole approximation, when an electron with angular momentum l is detached from an atom, the outgoing photoelectron carries an angular momentum of $l \pm 1$. If an electron is detached from an s atomic orbital ($l = 0$), the outgoing photoelectron will have $l = 1$ (pure p-wave) with $\beta = 2$. If an electron is detached from an atomic p orbital, the outgoing electron will carry s + d partial waves with $\beta = -1$.[21] While the β value is non-trivial to interpret for electron detachment from molecular orbitals (MOs),[22] it provides qualitative information about the symmetries of the MOs.

2.2. Theoretical methods

We employed the ABCluster software to perform the global minimum search.[23] Several initial structures were optimized using density functional theory (DFT) at the B3LYP/6-311+G* (ref. 24) level with the Gaussian 09 package.[25] Additional calculations were also done at the TPSSh/aug-cc-pVTZ level of theory.[26] Frequency calculations were carried out to compare with the experimental data and to ensure that the optimized structures were true minima. To account for SO interactions, we first utilized the state-averaged (SA)-complete active space self-consistent field (CASSCF) method[27] followed by multi-reference configuration interaction (MRCI) calculations[28] to get the low-lying electronic states. An active space consisting of 17 electrons and 9 orbitals was chosen for both PB_2O and AsB_2O. Then we carried out SO coupling calculations using the Breit-Pauli Hamiltonian in Molpro.[29,30] The aug-cc-pVTZ basis set was applied for the SO coupling calculations. Franck–Condon (FC) factors were computed using the ezFCF program.[31] Chemical bonding analyses were done using adaptive natural density partitioning (AdNDP).[32]

3. Experimental and theoretical results

3.1. Experimental results

High-resolution PEI data of cryogenically cooled PB_2O^- at 3.809 eV and 4.023 eV are shown in Fig. 1. The 4.023 eV spectrum (Fig. 1b) reveals two prominent peaks, X and A, which have similar intensities and are followed by numerous weak vibrational features labelled as peaks a–j. In the 3.809 eV spectrum (Fig. 1a), peaks a–f are better resolved, revealing that peaks X and A, as well as the pairs of a and b, c and d, and e and f, all have similar spacings and intensity patterns. It turns out that peaks g and h, and peaks i and j in the 4.023 eV spectrum, are similar pairs. These observations suggest that the pairs of peaks originate from two electronic states with parallel potential energy surfaces, likely corresponding to two SO-split states. Peaks X and A should be the 0–0 transitions to the two SO states of the neutral PB_2O molecule. Peak X defines an accurate electron affinity (EA) of 3.592 eV for PB_2O, while the spacing between X and A yields a SO splitting energy of 153 cm^{-1}. The presence of SO splitting suggests that PB_2O^- and PB_2O should have linear structures and the HOMO of PB_2O^- must be a π orbital.

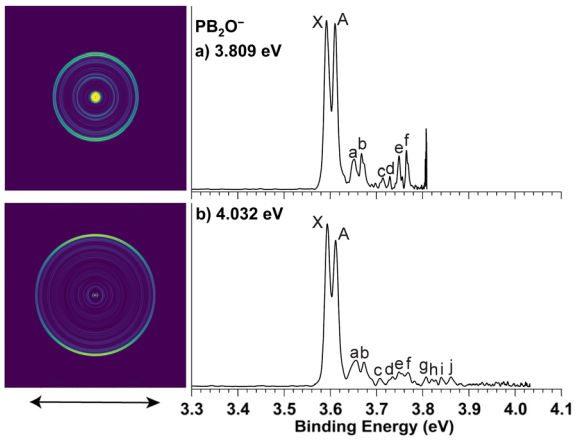

Fig. 1 Photoelectron images and spectra of cryogenically cooled PB_2O^- at (a) 3.809 eV and (b) 4.032 eV. The double arrow below the image indicates the laser polarization.

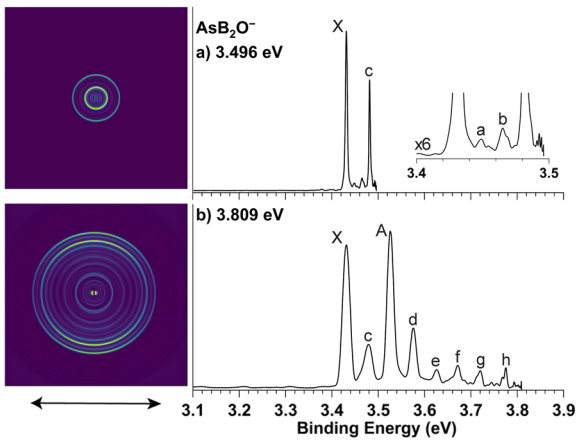

Fig. 2 Photoelectron images and spectra of cryogenically cooled AsB_2O^- at (a) 3.496 eV and (b) 3.809 eV. The double arrow below the image indicates the laser polarization.

The photoelectron angular distributions provide further insights into the nature of the HOMO, from which an electron is detached. In the 4.023 eV spectrum, all peaks exhibit s + d-type angular distributions, indicating that they are due to electron detachment from a π-type MO. At the lower photon energy of 3.809 eV, peaks that are closer to the detachment threshold, such as e and f, exhibit more isotropic angular distributions, due to the significant suppression of higher-order partial waves near the detachment threshold. The binding energies of all the observed peaks, their shifts relative to peaks X and A, and the assignments are given in Table 1.

High-resolution PEI data of cryogenically cooled AsB_2O^- at 3.496 eV and 3.809 eV are shown in Fig. 2. The 3.809 eV spectrum (Fig. 2b) reveals two strong peaks X and A, similar to those observed in PB_2O^-. Peaks c, e and f, and peaks d, g and h form two sets of similar vibrational progressions following peaks X and A. In addition to the better resolved peaks X and c, the 3.496 eV spectrum (Fig. 2a) also reveals two very weak peaks, a and b. The overall similarity between the spectra of AsB_2O^- and PB_2O^- suggests that AsB_2O^- also adopts a linear structure, with peaks X and A being the 0–0 transitions to two SO states. Peak X defines an accurate EA of 3.432 eV for AsB_2O, and the spacing between peaks X and A gives a SO splitting of 758 cm^{-1}. As expected from the periodic trend from P to As, the EA of AsB_2O decreases and the SO effect increases. All the resolved peaks for AsB_2O in the 3.809 eV spectrum display s + d-type angular distributions and become more isotropic in the near-threshold spectrum at 3.496 eV, similar to the observation in the spectra of PB_2O. The binding energies of all the observed peaks, their shifts relative to peaks X and A, and the assignments are given in Table 2.

Table 1 The measured binding energies (BE), assignments, and shifts relative to peaks X and A for the fine features observed in the spectra of PB_2O^-

	BE (eV)[a]	Assignment	Shift (cm^{-1})	
X	3.592(1)	$^2\Pi_{3/2}$ (0_0^0)	0	
A	3.611(1)	$^2\Pi_{1/2}$ (0_0^0)	153	0
a	3.651(1)	$^2\Pi_{3/2}$ (3_0^1)	476	
b	3.668(1)	$^2\Pi_{1/2}$ (3_0^1)		460
c	3.714(1)	$^2\Pi_{3/2}$ (3_0^2)	984	
d	3.729(1)	$^2\Pi_{1/2}$ (3_0^2)		952
e	3.749(1)	$^2\Pi_{3/2}$ (2_0^1)	1266	
f	3.765(1)	$^2\Pi_{1/2}$ (2_0^1)		1245
g	3.807(1)	$^2\Pi_{3/2}$ ($3_0^1 2_0^1$)	1734	
h	3.825(3)	$^2\Pi_{1/2}$ ($3_0^1 2_0^1$)		1726
i	3.840(1)	$^2\Pi_{3/2}$ (1_0^1)	2000	
j	3.862(1)	$^2\Pi_{1/2}$ (1_0^1)		2024

[a] The numbers in the parentheses represent the uncertainty in the last digit.

3.2. Theoretical results

The global minimum (GM) structures and low-lying isomers of PB_2O^- and AsB_2O^- are presented in Fig. S1.† The GM structures

Table 2 The measured binding energies (BE), assignments, and shifts relative to peaks X and A for the fine features observed in the spectra of AsB_2O^-

	BE (eV)[a]	Assignment	Shift (cm^{-1})	
X	3.432(1)	$^2\Pi_{3/2}$ (0_0^0)	0	
a	3.449(1)	$^2\Pi_{3/2}$ (4_0^1)	137	
b	3.465(1)	$^2\Pi_{3/2}$ (4_0^2)	266	
c	3.482(1)	$^2\Pi_{3/2}$ (3_0^1)	403	
A	3.526(1)	$^2\Pi_{1/2}$ (0_0^0)	758	0
		$^2\Pi_{3/2}$ (3_0^2)	758	
d	3.576(1)	$^2\Pi_{1/2}$ (3_0^1)		403
		$^2\Pi_{3/2}$ (2_0^1)	11615	
e	3.626(1)	$^2\Pi_{1/2}$ (3_0^2)		807
		$^2\Pi_{3/2}$ ($3_0^1 2_0^1$)	1565	
f	3.672(1)	$^2\Pi_{1/2}$ (2_0^1)		1178
		$^2\Pi_{3/2}$ (1_0^1)	1936	
g	3.719(1)	$^2\Pi_{1/2}$ ($3_0^1 2_0^1$)		1557
h	3.775(1)	$^2\Pi_{1/2}$ (1_0^1)		2008

[a] The numbers in the parentheses represent the uncertainty in the last digit.

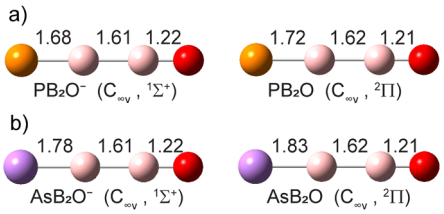

Fig. 3 The optimized structures of PB_2O^- and AsB_2O^- and the corresponding neutrals at the B3LYP/6-311+G* level. The point group symmetries and electronic states are also given. The bond lengths are given in Å.

of EB_2O^- (E = P, As) are found to have closed-shell linear structures with $C_{\infty v}$ symmetry and a $1\sigma^2 2\sigma^2 3\sigma^2 4\sigma^2 1\pi^4 5\sigma^2 2\pi^4$ ($^1\Sigma^+$) electronic configuration. All other isomers are much higher in energy. The optimized geometries at the B3LYP level for EB_2O^- and neutral EB_2O are shown in Fig. 3. The calculated vibrational frequencies of the neutral radicals are compared with the experimental values in Table 3. The results calculated at the TPSSh level agree well with those at the B3LYP level, as compared in Fig. S1 and S2 and Table S1.† The MOs for EB_2O^- are given in Fig. S3.† The HOMOs of EB_2O^- are π bonding orbitals essentially localized on the E–B bond. Detachment of an electron from the HOMO yields a $^2\Pi$ state for the neutral molecule with an electron configuration of $\ldots 1\pi^4 5\sigma^2 2\pi^3$. The $^2\Pi$ state splits into $^2\Pi_{3/2}$ and $^2\Pi_{1/2}$ due to SO coupling, with the $^2\Pi_{3/2}$ SO state being lower in energy. The calculated EAs to the $^2\Pi$ neutral ground state for both molecules at the B3LYP/6-311+G* level, in which SO coupling is not considered explicitly, are compared with the experimental values in Table 3. We computed the $^2\Pi$ state and an additional low-lying $^2\Sigma^+$ state using the SA3-CASSCF(17,9) and MRCI methods, and these states were included in the calculations of SO splitting between $^2\Pi_{1/2}$ and $^2\Pi_{3/2}$. The resulting SO splitting is computed to be 145 and 740 cm^{-1} for PB_2O and AsB_2O, respectively, as summarized in Table 3.

Table 3 The experimental EAs, spin–orbit (SO) splitting, and vibrational frequencies for EB_2O, compared with the calculated values

	EA (eV)[a]		SO splitting (cm^{-1})		Frequency (cm^{-1})[b]	
	Exp.	Cal.	Exp.	Cal.	Exp.[c]	Cal.
PB_2O	3.592	3.52	153	145	2010 (ν_1)	2010
					1260 (ν_2)	1254
					470 (ν_3)	472
AsB_2O	3.432	3.39	758	740	2000 (ν_1)	2003
					1165 (ν_2)	1161
					400 (ν_3)	389
					135 (ν_4)	143

[a] Spin–orbital coupling is not considered in the computed EAs. [b] Calculated frequencies are scaled by a factor of 0.97. ν_1 = B–O stretching, ν_2 = B–B stretching, ν_3 = E–B stretching, ν_4 = *cis*-bending. The scaling factor is based on the NIST computational chemistry comparison and benchmark database (https://cccbdb.nist.gov/vibscalejustx.asp). [c] The experimental uncertainty is estimated to be ±10 cm^{-1}.

4. Discussion

4.1. Comparison between experiment and theory

The calculated EAs for the linear structures, 3.52 eV for PB_2O and 3.39 eV for AsB_2O at the B3LYP level, are in good agreement with the experimental data of 3.592 eV and 3.432 eV, respectively. The computed SO splitting for the $^2\Pi$ state, 145 cm^{-1} for PB_2O and 740 cm^{-1} for AsB_2O, also agrees well with the spacing between peaks X and A: 153 cm^{-1} for PB_2O and 758 cm^{-1} for AsB_2O. The excellent agreement between theory and experiment confirms that peaks X and A indeed correspond to the two SO states and validates the linear structures of EB_2O^- (E = P, As).

To understand the observed vibrational structures, we computed the FC factors using the optimized geometries and vibrational frequencies at the B3LYP/6-311+G* level, as shown in Fig. 4, where the blue and red bars represent FC factors for transitions to the $^2\Pi_{3/2}$ and $^2\Pi_{1/2}$ states, respectively. The overall FC profiles agree well with the experimental spectra, further validating the linear structures. For detachment transitions from the linear anions to linear neutrals, FC-active modes can only involve stretching vibrations. In the case of PB_2O, we observed all three stretching modes, which are essentially the P–B, B–B, and B–O vibrations, designated as modes ν_3, ν_2, and ν_1 (Fig. S4†). Using the FC simulations, we can readily assign the observed vibrational peaks for PB_2O (Table 1). Peaks a and b correspond to ν_3 of the two SO states, while peaks c and d correspond to the overtone of ν_3 of the two SO states. Peaks *e* and *f* are from ν_2 of the two SO states. Peaks g and h represent the combination modes of ν_3 and ν_2 for the two SO states. Peaks i and j correspond to ν_1 of the two SO states.

In the spectra of AsB_2O^- (Table 2), peak *c* corresponds to excitation to the ν_3 mode of the $^2\Pi_{3/2}$ state, while its overtone overlaps with the 0–0 transition of the $^2\Pi_{1/2}$ state, resulting in peak A appearing slightly more intense than peak X. The ν_2 excitation of the $^2\Pi_{3/2}$ state also overlaps with the excitation of

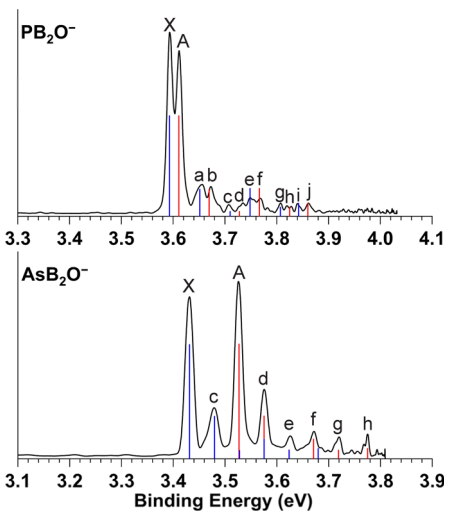

Fig. 4 Comparison of the calculated Franck–Condon factors (vertical lines) with the PE spectra of PB_2O^- at 4.032 eV and AsB_2O^- at 3.809 eV. The blue and red colours represent the Franck–Condon factors of the $^2\Pi_{3/2}$ and $^2\Pi_{1/2}$ states, respectively.

the ν_3 mode of the $^2\Pi_{1/2}$ state, causing peak d to appear slightly more intense than peak c. Peak e is the overlap of the overtone of ν_1 of the $^2\Pi_{1/2}$ state and the combination of ν_3 and ν_2 of the $^2\Pi_{3/2}$ state. Peak f is dominated by excitation to ν_2 of the $^2\Pi_{1/2}$ state with minor contribution from ν_1 of the $^2\Pi_{3/2}$ state. Peaks g and h are from the combination of ν_1 and ν_2 of the $^2\Pi_{1/2}$ state and ν_1 of the $^2\Pi_{1/2}$ state, respectively.

In the 3.496 eV spectrum of AsB_2O^- (Fig. 2a), two very weak peaks a and b are observed. These peaks do not correspond to any FC-active modes. Instead, their frequencies agree with the calculated fundamental and overtone of the *cis*-bending mode ν_4 (Fig. S4†). For linear molecules, overtones of bending modes are symmetry-allowed, while the fundamental of the bending mode is forbidden. In a previous PES study on $BiBH^-$,[10] which has a similar linear structure, we also found a weak bending vibrational feature attributed to vibronic coupling between the $^2\Pi$ state and a higher-lying $^1\Sigma^+$ excited state. The observation of the weak 4_0^1 bending feature in the spectrum of AsB_2O^- could also come from vibronic coupling.

4.2. Chemical bonding in PB_2O^- and AsB_2O^-

We analysed the chemical bonding in EB_2O^- using the AdNDP method (Fig. 5) and the MOs (Fig. S3†). The AdNDP results for EB_2O^- (E = P, As) are nearly identical. We can identify two lone pairs on E and O, a triple bond between E and B, a B–B single bond and another triple bond between B and O. Thus, the two EB_2O^- species are electron-precise molecules $[E{\equiv}B{-}B{\equiv}O]^-$. The triple bonds can also be readily seen from the HOMO and HOMO-1 (Fig. S3†), representing the E–B π and σ bonds, respectively. We calculated the Wiberg bond index matrix on the natural atomic orbital (NAO) basis. The Wiberg bond orders for the P≡B and As≡B bonds in PB_2O^- and AsB_2O^- are 2.84 and 2.83, respectively, consistent with the AdNDP and MO analyses. PB_2O^- and AsB_2O^- are the first molecules observed to contain P≡B and As≡B triple bonds. In the valence bond model, the B atom undergoes sp hybridization, where one of the sp hybridized orbitals forms a σ bond with BO and the other sp orbital forms another σ bond with P or As. The P and As atoms also undergo sp hybridization, so that the s orbital from P or As makes considerable contribution to the σ bond. One of the sp orbitals forms a σ bond with the B atom, and the other sp orbital gives rise to the lone pair on P/As. The calculated atomic orbital composition shows that the s orbital contributes 34% to the P sp hybridized orbitals, while it contributes 31% to the As sp hybridized orbitals. The $2p_x$ and $2p_y$ orbitals of B form two π bonds with the corresponding p orbitals of P or As, giving rise to the P≡B and As≡B triple bond. The contribution of the valence s orbital to the σ bond in P≡B and As≡B is quite different from the weak triple bond in Bi≡B, where the 6s orbital is basically a lone pair.[9,10] The strong relativistic effects significantly stabilize the 6s orbital relative to the 6p orbitals, making it unfavourable for sp hybridization.

The P–B and As–B bond lengths in PB_2O^- and AsB_2O^- are also consistent with their triple bond nature. According to Pyykko's additive covalent radii,[33] the P≡B and As≡B triple bond lengths are 1.67 Å and 1.79 Å, respectively, in excellent agreement with the calculated P–B and As–B bond lengths of 1.68 Å and 1.78 Å in PB_2O^- and AsB_2O^- (Fig. 3). In the PB_2O and AsB_2O neutrals, removal of an electron from the π bonding orbital (HOMO in Fig. S3†) weakens the P–B and As–B bonds, resulting in a bond order of 2.5. Consequently, the P–B and As–B bond lengths in the neutral species increase to 1.72 Å and 1.83 Å, respectively, indicating the significant strength of the π bond in PB_2O^- and AsB_2O^-. It should be noted that the P–B bond length in PB_2O is consistent with that in the linear PBH (1.72 Å) species observed in a low temperature matrix, where the P–B bond order is also 2.5.[17] It is interesting to point out that the sp lone pair on the terminal P or As atoms in PB_2O^- and AsB_2O^- may be able to coordinate to a bulky Lewis acid to allow the isolation of the first P≡B and As≡B triple bonds.

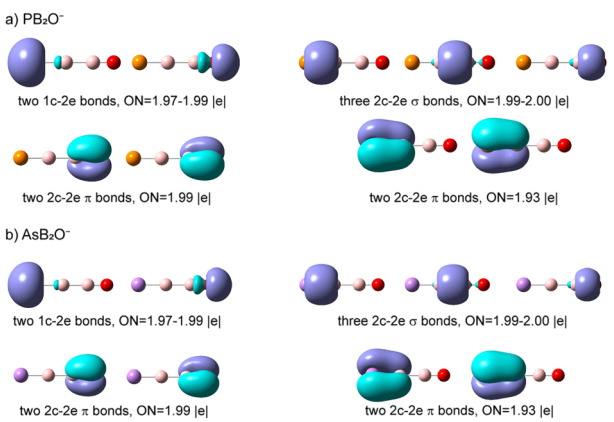

Fig. 5 AdNDP chemical bonding analyses for (a) PB_2O^- and (b) AsB_2O^-.

5. Conclusion

In conclusion, we report a high-resolution photoelectron imaging investigation of PB_2O^- and AsB_2O^-. The electron affinities of neutral PB_2O and AsB_2O are measured to be 3.592 eV and 3.432 eV, respectively. Vibrationally resolved photoelectron imaging, combined with computational chemistry, confirms that PB_2O^- and AsB_2O^- have linear structures, $[P{\equiv}B{-}B{\equiv}O]^-$ and $[As{\equiv}B{-}B{\equiv}O]^-$, with P≡B and As≡B triple bonds. Both PB_2O^- and AsB_2O^- are closed-shell with a $^1\Sigma^+$ electronic state, whereas their neutrals are open shell with a $^2\Pi_{3/2}$ ground state. The spin–orbit split $^2\Pi_{1/2}$ excited state is determined to be 153 cm^{-1} and 758 cm^{-1} higher in energy for PB_2O and AsB_2O, respectively. The PB_2O^- and AsB_2O^- species represent the first molecules containing P≡B and As≡B triple bonds, which can serve as benchmarks for studying P–B and As–B multiple bonds and may be viable for bulk syntheses.

Data availability

The data that supports the findings of this study is available from the corresponding author upon request.

Author contributions

H. W. G. and J. H. did the experiment. H. W. G. analysed the data and wrote the first draft of the manuscript. J. H. did the

calculations. L. S. W. guided and advised the project, and revised and finalized the manuscript.

Conflicts of interest

There are no conflicts to declare.

Acknowledgements

This work was supported by the U.S. National Science Foundation (Grant No. CHE-2403841). The calculations were performed using resources at the Centre for Computation and Visualization (CCV) of Brown University.

References

1 (*a*) A. W. Ehlers, E. V. Barends, F. M. Bickelhaupt and U. Radius, *Chem.–Eur. J.*, 1998, **4**, 210; (*b*) D. Vidovic, G. A. Pierce and S. Aldridge, *Chem. Commun.*, 2009, 1157; (*c*) H. Braunschweig, R. D. Dewhurst and V. H. Gessner, *Chem. Soc. Rev.*, 2013, **42**, 3197; (*d*) M. Soleilhavoup and G. Bertrand, *Angew. Chem., Int. Ed.*, 2017, **56**, 10282.

2 (*a*) H. Braunschweig, C. Kollann and U. Englert, *Angew. Chem., Int. Ed.*, 1998, **37**, 3179; (*b*) A. H. Cowley, V. Lomelf and A. Voigt, *J. Am. Chem. Soc.*, 1998, **120**, 6401.

3 (*a*) H. Braunschweig, M. Colling, C. Kollann, H. G. Stammler and B. Neumann, *Angew. Chem., Int. Ed.*, 2001, **40**, 2298; (*b*) D. L. Coombs, S. Aldridge, C. Jones and D. J. Willock, *J. Am. Chem. Soc.*, 2003, **125**, 6356; (*c*) D. L. Coombs, S. Aldridge, A. Rossin, C. Jones and D. J. Willock, *Organometallics*, 2004, **23**, 2911; (*d*) H. Braunschweig, M. Burzler, T. Kupfer, K. Radacki and F. Seeler, *Angew. Chem., Int. Ed.*, 2007, **46**, 7785; (*e*) H. Braunschweig, K. Radacki and K. Uttinger, *Angew. Chem., Int. Ed.*, 2007, **46**, 3979; (*f*) B. Blank, M. Colling-Hendelkens, C. Kollann, K. Radacki, D. Rais, K. Uttinger, G. R. Whittell and H. Braunschweig, *Chem.–Eur. J.*, 2007, **13**, 4770; (*g*) H. Braunschweig, M. Forster, T. Kupfer and F. Seeler, *Angew. Chem., Int. Ed.*, 2008, **47**, 5981; (*h*) G. Alcaraz, U. Helmstedt, E. Clot, L. Vendier and S. Sabo-Etienne, *J. Am. Chem. Soc.*, 2008, **130**, 12878; (*i*) S. Bertsch, H. Braunschweig, B. Christ, M. Forster, K. Schwab and K. Radacki, *Angew. Chem., Int. Ed.*, 2010, **49**, 9517.

4 M. J. Drance, J. D. Sears, A. M. Mrse, C. E. Moore, A. L. Rheingold, M. L. Neidig and J. S. Figueroa, *Science*, 2019, **363**, 1203.

5 T. Chen, L. F. Cheung, W. J. Chen, J. Cavanagh and L. S. Wang, *Angew. Chem., Int. Ed.*, 2020, **59**, 15260.

6 L. F. Cheung, T. T. Chen, G. S. Kocheril, W. J. Chen, J. Czekner and L. S. Wang, *J. Phys. Chem. Lett.*, 2020, **11**, 659.

7 (*a*) M. Zhou, N. Tsumori, Z. Li, K. Fan, L. Andrews and Q. Xu, *J. Am. Chem. Soc.*, 2002, **124**, 12936; (*b*) H. Brauschweig, R. D. Dewhurst, K. Hammond, J. Mies, K. Radacki and A. Vargas, *Science*, 2012, **336**, 1420.

8 S. D. Li, H. J. Zhai and L. S. Wang, *J. Am. Chem. Soc.*, 2008, **130**, 2573.

9 T. Jian, L. F. Cheung, T. T. Chen and L. S. Wang, *Angew. Chem., Int. Ed.*, 2017, **56**, 9551.

10 H. W. Gao, J. Hui and L. S. Wang, *Chem. Commun.*, 2023, **59**, 12431.

11 (*a*) P. Paetzold, A. Richter, T. Thijssen and S. Würtenberg, *Chem. Ber.*, 1979, **112**, 3811; (*b*) J. Wang, P. Jia, W. Sun, Y. Wei, Z. Lin and Q. Ye, *Inorg. Chem.*, 2022, **61**, 8879.

12 R. C. Fischer and P. P. Power, *Chem. Rev.*, 2010, **110**, 3877.

13 J. D. Watts and L. C. V. Zant, *Chem. Phys. Lett.*, 1996, **251**, 119.

14 P. P. Power, *Nature*, 2010, **463**, 171–177.

15 (*a*) E. Rivard, W. A. Merrill, J. C. Fettinger, R. Wolf, G. H. Spikes and P. P. Power, *Inorg. Chem.*, 2007, **46**, 2971; (*b*) J. Li, Z. Lu and L. L. Liu, *J. Am. Chem. Soc.*, 2022, **144**, 23691; (*c*) A. Koner, B. Morgenstern and D. M. Andrada, *Angew. Chem., Int. Ed.*, 2022, **61**, e202203345; (*d*) E. Rivard, W. A. Merrill, J. C. Fettinger and P. P. Power, *Chem. Commun.*, 2006, **36**, 3800; (*e*) M. Wen, R. Medel, P. V. Zasimov, C. Müller and S. Riedel, *Chem. Sci.*, 2024, **15**, 8045; (*f*) E. A. LaPierre, B. O. Patrick and I. Manners, *J. Am. Chem. Soc.*, 2023, **145**, 7107.

16 J. S. Lu, M. C. Yang and M. D. Su, *ACS Omega*, 2018, **3**, 76.

17 L. Wang, X. Jiang, G. Wang, X. Zeng and M. Zhou, *Chem.–Eur. J.*, 2023, **29**, e202203704.

18 I. León, Z. Yang, H. T. Liu and L. S. Wang, *Rev. Sci. Instrum.*, 2014, **85**, 083106.

19 (*a*) G. S. Kocheril, H. W. Gao, D. F. Yuan and L. S. Wang, *J. Chem. Phys.*, 2022, **157**, 171101; (*b*) G. S. Kocheril, H. W. Gao and L. S. Wang, *Mol. Phys.*, 2024, **122**, e2182610; (*c*) G. S. Kocheril, H. W. Gao and L. S. Wang, *J. Chem. Phys.*, 2023, **158**, 236101; (*d*) H. W. Gao, H. W. Choi, J. Hui, W. J. Chen, G. S. Kocheril and L. S. Wang, *J. Chem. Phys.*, 2023, **159**, 114301; (*e*) H. W. Gao, H. W. Choi, J. Hui and L. S. Wang, *J. Phys. Chem. A*, 2024, **128**, 3579.

20 B. Dick, *Phys. Chem. Chem. Phys.*, 2019, **21**, 19499.

21 J. Cooper and R. N. Zare, *J. Chem. Phys.*, 1968, **48**, 942.

22 A. Sanov and R. Mabbs, *Int. Rev. Phys. Chem.*, 2008, **27**, 53.

23 J. Zhang and M. Dolg, *Phys. Chem. Chem. Phys.*, 2015, **17**, 24173.

24 C. T. Lee, W. T. Yang and R. G. Parr, *Phys. Rev. B:Condens. Matter Mater. Phys.*, 1988, **37**, 785.

25 M. J. Frisch *et al.*, *Gaussian 09, Revision A.1*, Gaussian, Inc., Wallingford, CT, 2009.

26 J. Tao, J. P. Perdew, V. N. Staroverov and G. E. Scuseria, *Phys. Rev. Lett.*, 2003, **91**, 146401.

27 H. J. Werner and P. J. Knowles, *J. Chem. Phys.*, 1985, **82**, 5053.

28 H. J. Werner and P. J. Knowles, *J. Chem. Phys.*, 1988, **89**, 5803.

29 A. Berning, M. Schweizer, H. J. Werner, P. J. Knowles and P. Palmieri, *Mol. Phys.*, 2000, **98**, 1823.

30 H. J. Werner *et al.*, MOLPRO, a package of *ab initio* programs, see **http://www.molpro.net**.

31 S. Gozem and A. I. Krylov, *WIREs Comp. Mol. Sci.*, 2021, **12**, e1546.

32 D. Y. Zubarev and A. I. Boldyrev, *Phys. Chem. Chem. Phys.*, 2008, **10**, 5207.

33 P. Pyykko, *J. Phys. Chem. A*, 2015, **119**, 2326.